From intracluster medium dynamics to particle acceleration

Zhang, X.

1 | Introduction

1.1 Galaxy clusters and the intracluster medium

Back to the 18th century, Charles Messier compiled his illustrious catalog of nebulae and stellar clusters (Messier 1781) and noticed the concentration of 'nebulae' in the Virgo constellation. Almost at the same time, Wilhelm Herschel published his famous work on mapping the structure of the Universe (Herschel 1785), where he described the Coma Cluster as 'nebulous stratum'. The nature of this type 'nebulae' was disclosed one hundred years later by Hubble (1929) as galaxies outside our Milky Way. A few years later, Zwicky (1933) first estimated the mass of the Coma Cluster using the velocity dispersion of member galaxies and first proposed the idea of dark matter to account for the missing mass in galaxy clusters. In 1958, a well known optical catalog of galaxy clusters was published by Abell (1958), where clusters are divided into 6 richness classes based on the number of member galaxies. A review by Biviano (2000) explicitly covers the early day research on galaxy clusters until the departure of George Abell in 1983.

Modern observational, theoretical and numerical simulation works on cosmology build up a grand picture of the structure formation. In this picture, the large scale structure (LSS) is formed hierarchically by the collapse of gravitationally bound overdensities from the initial density perturbation field. The nodes of the cosmic web, which are gravitationally bound, are termed as *halos*, where dark matter is the predominant mass content. In the hierarchical formation, halos of galaxies are formed first, followed by galaxy groups. The most massive halos, galaxy clusters, are formed at $z \lesssim 2$, corresponding to a lookback time of $t \sim 10.5\,\mathrm{Gyr}$ based on a consensus concordance ΛCDM cosmology. The halos of galaxy clusters are still
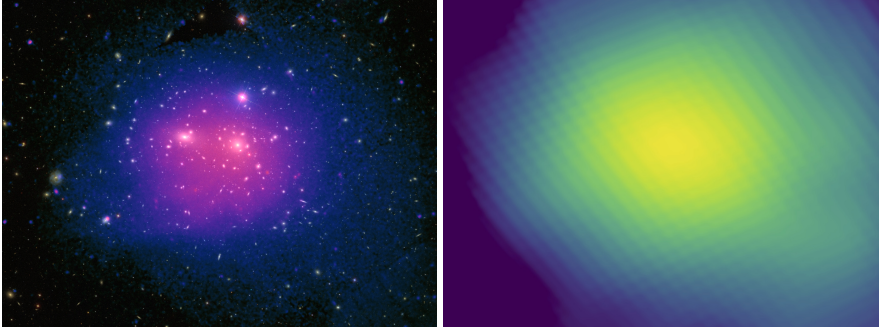
Figure 1.1: *Left*: Optical and X-ray composite image of the Coma Cluster. The yellows spots are individual galaxies in optical and the blue to magenta color is the ICM in X-rays. *Right*: *Planck* SZ map of the same sky region. Image credit: ESA/XMM-Newton/SDSS/Jeremy Sanders/Planck.

growing through cosmic accretion and mergers. See Kravtsov & Borgani (2012) for a review on galaxy cluster formation. In the context of structure formation, the cosmological parameters, such as density fractions of baryonic matter, dark matter and dark energy, and the dark energy equation of state determine the growth of the LSS. Therefore, galaxy clusters are one of the important probes for constraining the properties of our Universe, see Allen et al. (2011) for a review on observational cosmology using galaxy clusters.

Beside the macroscopic view of structure formation, galaxy clusters are key laboratories for studying the physics of space plasma. The intracluster medium (ICM), which is observed as a gaseous halo in X-rays (see Fig. 1.1), contributes the major proportion of baryonic matter. The ICM has several extreme properties among all forms of space plasma: 1) it fills the whole dozens Mpc^3 volume inside the accretion radius of the cluster; 2) it has low densities ranging from $\sim 10^{-5}$ cm^{-3} in the outskirts to $\sim 10^{-2}$ cm^{-3} at the center; 3) it has a high temperature of about a few keV ($\sim 10^7$–10^8 K), where H and He are totally ionized; 4) the magnetic field strength in the ICM is weak, usually a few μG, resulting a high plasma β_{pl} parameter[1] > 100.

The tenuous and extreme hot nature of the ICM makes it optically thin and X-ray bright, and it is in collisional ionization equilibrium (CIE). The main radiative processes are thermal bremsstrahlung for the continuum

---

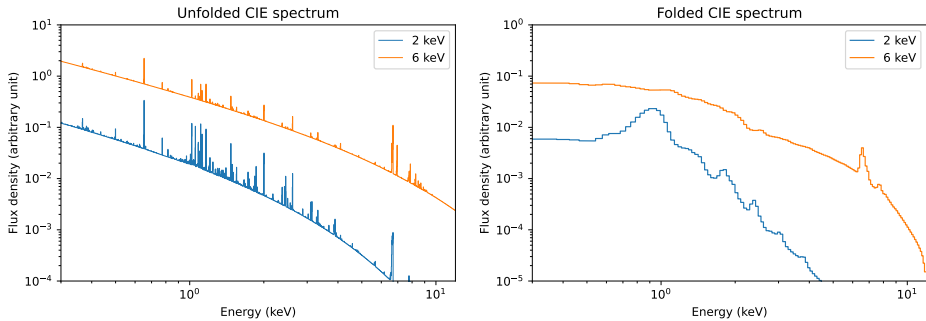[1] $\beta_{\mathrm{pl}} \equiv p_{\mathrm{gas}}/p_{\mathrm{B}}$

Figure 1.2: *Left*: CIE spectra for a 2 keV and a 6 keV plasma, respectively. The spectra are calculated based on the SPEXACT 3.06.01 database with a 0.3 proto-solar abundance (Lodders et al. 2009). *Right*: The same spectra as in the left panel but folded by the EPIC-pn instrumental response.

and excitation processes from highly ionized metal elements for the line emission. For low mass clusters where the temperature is relatively low, other processes such as recombination and two-photon emission are also important for continuum emission (see Kaastra et al. 2008 for a review on the thermal radiative processes). Examples of CIE spectra at temperatures of 6 keV and 2 keV are plotted in Fig. 1.2. The two spectra show different features, especially after being convolved with the instrumental responses (here *XMM-Newton* European Photon Imaging Camera (EPIC) pn for example). The main feature in a $kT = 2$ keV spectrum is the Fe L-shell complex around 1 keV energy, while in a $kT = 6$ keV spectrum, the main feature is the Fe He-α line at 6.7 keV.

In addition to the X-ray emission, which directly reflects the density and temperature of the ICM, the pressure of the ICM can be learned from the Sunyaev-Zeldovich (SZ) effect (Sunyaev & Zeldovich 1972), which is the distortion of the cosmic microwave background (CMB) due to its inverse Compton scattering with the ICM electrons.

1.1.1 X-ray instruments and observations

The current generation of X-ray missions adopt Wolter-I (Wolter 1952) grazing incidence optics for the mirror and use silicon charge-coupled device (CCD) arrays as the detector. The Wolter-I optics consist of a parabolic surface followed by a hyperbolic surface. This design allows a mirror module

3

to have multiple nested mirror shells to increase the collecting power to a few hundred cm^2 for X-rays below 2 keV energy. The CCD array can host millions of pixels with a pixel size of dozens of microns to cover a certain area of the sky. The disadvantage of CCD detectors is their relatively low energy resolution (see the right panel of Fig. 1.2 for example), which is unable to resolve individual lines.

For sources like galaxy clusters, due to the low photon flux, there will be no more than one photon collected by the detector at the same pixel location within a frame time. In this way, both the coordinate and energy of each individual collected photon can be measured, and these detectors are known as imaging spectrometers, such as the EPIC on *XMM-Newton* and the Advanced CCD Imaging Spectrometer (ACIS) on *Chandra*. Observations of galaxy clusters using X-ray imaging spectrometers allow us to have both spatial and spectral information of the ICM emission. With the hundred eV energy resolution of the CCD and the sub-arcmin spatial resolution of the telescopes, thermodynamic structures in both relaxed clusters and disturbed merging clusters have been well explored over the last two decades.

Alternatively, like other electromagnetic waves at lower frequencies, X-ray photons show wave properties. A diffraction grating behind the mirror can disperse the X-ray photons. The dispersed photons with different energy are then located at different positions on the detector array. This method can achieve a much higher spectral resolution $E/\Delta E$ of a few thousand for point-like sources. This type of instruments is therefore known as grating spectrometers, such as the two Reflection Grating Spectrometer (RGS) on *XMM-Newton*, the High Energy Transmission Grating (HETG) and the Low Energy Transmission Grating (LETG) on *Chandra*. For galaxy clusters, only the bright compact cores of relaxed clusters can be observed using grating spectrometers, whereas the observed spectral resolution is still degraded due to the diffuse nature of the ICM, and imaging is not possible with this type of technology.

The performance of the most widely used X-ray telescopes and the onboard imaging spectrometers are listed in Table 1.1.

1.2   Gas motions in the ICM

Throughout the ~ 10 Gyr lookback time since the first cluster formation, galaxy clusters grow by accretion of the intergalactic medium and hierar-

Table 1.1: Comparison of the most widely used X-ray telescopes and the onboard imaging spectrometer for the ICM study.

Telescope	HEW[a] ($''$)	Instrument	A_{eff}[b] (cm^2)	FoV	ΔE[c] (eV)
XMM-Newton	15	EPIC-MOS 1,2	500	$\varnothing = 30'$	150
		EPIC-pn	1300		
Chandra	0.5	ACIS-I	600[*]/300[†]	$16.9' \times 16.9'$	280
		ACIS-S	750[*]/400[†]	$8.3' \times 8.3'$	150
Suzaku	110	XIS 0,2,3	330	$18' \times 18'$	140
		XIS 1	370		

[a] Half energy width.
[b] At 1.5 keV.
[c] At 5.9 keV.
[*] After launch.
[†] In 2022.

chical mergers. Meanwhile, on smaller scales, the accretion of mass onto the supermassive black holes hosted by the central brightest cluster galaxies (BCGs) trigger energetic active galactic nuclei (AGN) outbursts. All these processes drive gas motions in the ICM, though with different observational features. This thesis mainly focuses on the gas motions on large scales and therefore we will not discuss the gas motions due to AGN feedback.

Fig. 1.3 shows the ICM turbulent velocity field in a numerical simulation (Vazza et al. 2017), where turbulence fills the entire volume inside the accretion shock. Most of the turbulence is solenoidal ($\nabla \cdot \vec{v} = 0$), while a small fraction is compressive ($\nabla \times \vec{v} = 0$). The compressive component is mostly in layers at different radii, which trace shocks, including outer cosmic accretion shocks and inner merging shocks.

1.2.1 Shocks and cold fronts as evidence of ICM dynamics

Major and minor mergers can both drive ICM bulk motions, but in different ways. Shocks and cold fronts are the two evident signatures of ICM bulk motions and are widely observed in both relaxed and merging systems (Markevitch & Vikhlinin 2007).
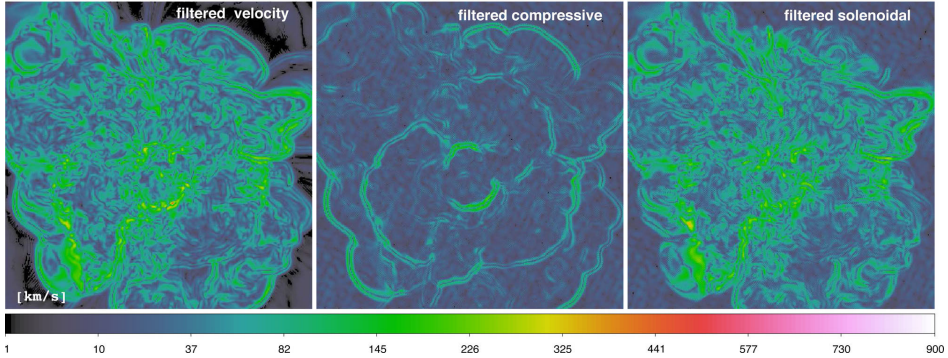
Figure 1.3: The ICM turbulent velocity field of a $M_{\text{tot}} = 10^{14}\ M_\odot$ cluster in a cosmological simulation (Vazza et al. 2017). The box size is 5.8 Mpc^3. The *Middle* and *Right* panels show the compressive and solenoidal components, respectively. Image credit: Franco Vazza.

Major mergers are the collisions of two (or more) halos with mass ratio < 10, and are the most energetic events in the Universe, releasing $> 10^{64}$ erg energy. Gravitational potential energy is first converted to kinetic energy of the two halos. The collision velocity can be up to a few thousand km s^{-1}, exceeding the local sound speed (see Eq. 1.1). As a result, pairs of Mpc scale merging shocks are generated, see the innermost pair in the middle panel of Fig. 1.3 as an example in simulations. In the same process, if one of the subclusters has a dense cool core, an additional interface will be created between the decelerated post-shock flow and the core, which is named a cold front. Cold front is originally a meteorological terminology, representing the transition zone between warm air and cold air. In ICM astrophysics, it represents the subsonic and isobaric interface between ICM gas with two different temperatures. Bow shock - cold front patterns are frequently observed in merging systems, e.g. the Bullet Cluster (Markevitch et al. 2002), Abell 2146 (Russell et al. 2010, 2012) and Abell 3376 (Urdampilleta et al. 2018). Due to the longer thermal diffusion timescale compare to the pressure equilibrium timescale at the interface (Vikhlinin et al. 2001; Markevitch et al. 2003), the ICM shows clear stratification with cold dense gas on the one side and hot diluted gas on the other side.

Minor mergers (mass ratio > 10), which take place more frequently during the structure formation, drive bulk motions in different ways. When the impact factor is small, i.e. the subhalo directly falls into the major halo, a

similar bow shock - cold front pattern will be generated if the falling speed exceeds the local sound speed, e.g. M89 in the Virgo Cluster (Kraft et al. 2017). On the contrary, when the impact factor is large, i.e. the subhalo is flying by or falling through an orbital trajectory, if the major cluster has a dense cool core, the core will suffer from the gravitational perturbation from the subhalo. The perturbation is not strong enough to entirely pull the core out of the bottom of the gravitational well, but can displace the core and make it move around within the central region. A cold front is created between the displaced central cool gas and the ambient hot gas. This cold front will evolve to spiral shapes and is named a 'sloshing' cold front (Markevitch et al. 2001).

In addition to the obvious X-ray surface brightness (SB) discontinuities, major mergers and sloshing will also generate turbulence. Theoretical works (Schekochihin & Cowley 2006; Melville et al. 2016) and observations of different aspects (Ichinohe et al. 2017; Kraft et al. 2017; Zhuravleva et al. 2019) suggest that the magnetized ICM has a large effective Reynolds number, i.e. the ratio of kinetic energy to viscous damping in a fluid flow. The high Reynolds number implies the presence of turbulent motions in the ICM. Though there is not enough direct observational evidence (the indirect evidence and methods will be discussed later in Sect. 1.2.2), numerical simulations already show that ICM can be generated by cosmic accretion, mergers, and sloshing (Vazza et al. 2009; van Weeren et al. 2012; ZuHone et al. 2013; Nelson et al. 2014; Vazza et al. 2017).

1.2.2 Quantifying ICM gas motions

Different from some other variable astronomical objects, e.g. AGNs, variable stars, supernovae, etc., the timescales of different processes in the ICM are mostly $> 10^8$ yrs. Therefore, we are unable to observe the temporal evolution of the ICM. Quantifying ICM gas motions is based on imaging and spectroscopic analyses, i.e. studying the SB, emission lines and continuum properties. A detailed review on this topic is presented by Simionescu et al. (2019). In this section, we focus on the shock speed and turbulent velocity dispersions in the ICM.

Shock speed

From the shock Mach number definition $\mathcal{M}_{\mathrm{shock}} \equiv v_{\mathrm{shock}}/c_{\mathrm{s}}$, where v_{shock} is the shock speed and c_{s} the sound speed in the pre-shock region, quanti-
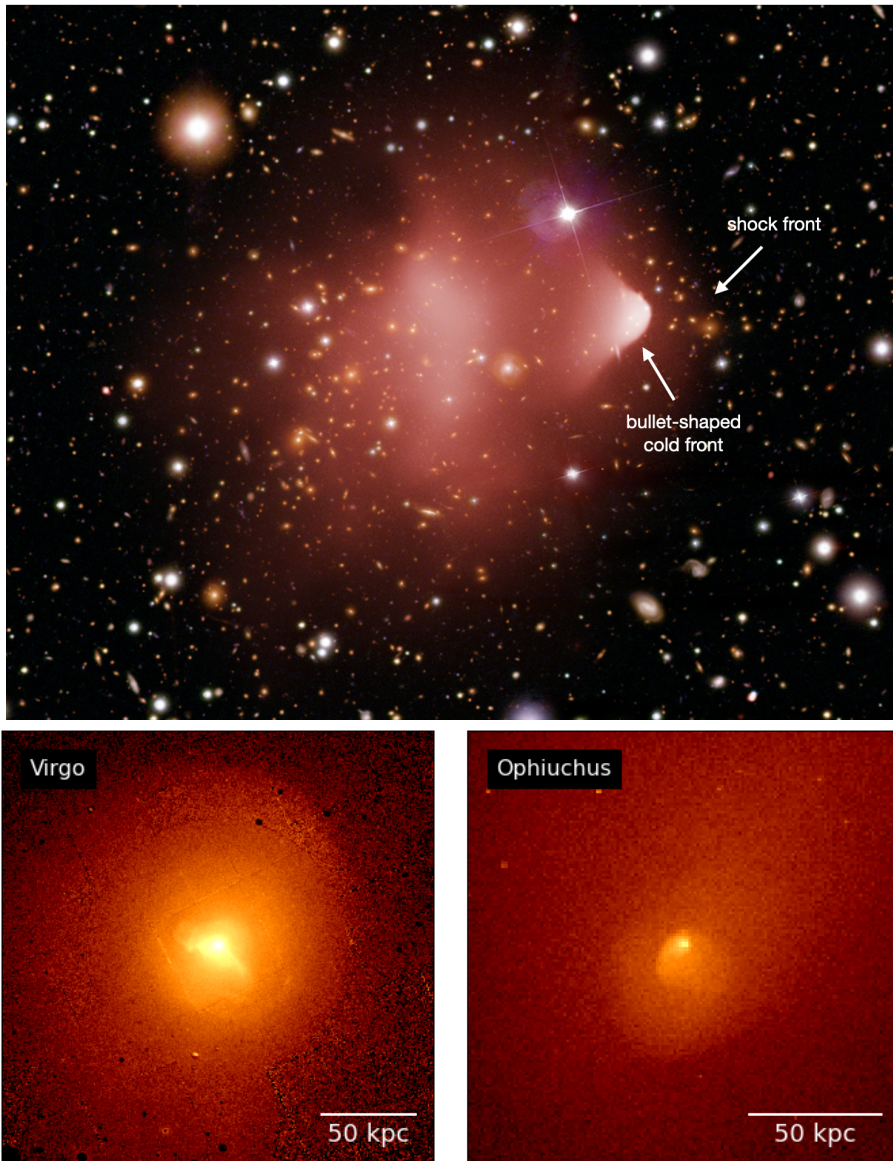
Figure 1.4: Gallery of shocks and cold fronts. *Top*: Optical and X-ray composite image of the Bullet Cluster, which shows a textbook bow shock - cold front pattern. Image credit: NASA/CXC/CfA/M.Markevitch et al./STScI; Magellan/U.Arizona/D.Clowe et al. *Bottom Reft* and *Bottom Right*: Sloshing cold fronts in the Virgo Cluster and the Ophiuchus Cluster, respectively. The two images are adapted from ZuHone & Su (2022) and are originally from Simionescu et al. (2010) and Giacintucci et al. (2020).

fying shock speed needs the measurements of c_s and $\mathcal{M}_\mathrm{shock}$. The former quantity depends on the temperature of the ICM,

$$c_\mathrm{s} = \sqrt{\frac{\gamma kT}{\mu m_\mathrm{p}}}, \tag{1.1}$$

where $\gamma = 5/3$ for an ideal gas. The shock Mach number can be quantified based the Rankine-Hugoniot condition (Macquorn Rankine 1870; Landau & Lifshitz 1959),

$$\mathcal{M}_\mathrm{shock} = \left[\frac{2C}{\gamma + 1 - C(\gamma - 1)}\right]^2, \tag{1.2}$$

where $C \equiv n_\mathrm{post}/n_\mathrm{pre}$, the density ratio across the shock. Alternatively, the temperature jump can also be a proxy of Mach number,

$$\frac{kT_\mathrm{post}}{kT_\mathrm{pre}} = \frac{(\gamma + 1)/(\gamma - 1) - C^{-1}}{(\gamma + 1)/(\gamma - 1) - C}, \tag{1.3}$$

where kT_post and kT_pre are the temperature in the post-shock and pre-shock regions, respectively.

The ICM density profile at a large radius can be approximated as a power law. Based on this, a practical way to measure the density jump of a spherical shock is using a double power-law density model to forward fit the surface brightness profile. The number density profile can be expressed as

$$n(r) = \begin{cases} C \times n_0 \left(\dfrac{r}{r_\mathrm{shock}}\right)^{-\alpha_1} & \text{when } r \leqslant r_\mathrm{shock}, \\[2ex] n_0 \left(\dfrac{r}{r_\mathrm{shock}}\right)^{-\alpha_2} & \text{when } r > r_\mathrm{shock}, \end{cases} \tag{1.4}$$

where n_0 the density normalization, r_shock the shock location, α_1 and α_2 the post and pre-shock power law indices, respectively. The corresponding surface brightness profile is

$$S(r) \propto \int_{-\infty}^{\infty} \left[n\left(\sqrt{l^2 + r^2}\right)\right]^2 \mathrm{d}l, \tag{1.5}$$

where l is the line-of-sight (LOS) coordinate. This method has several caveats that may lead to over- or underestimations of the density jump.

First, it can only be used for a shock where the temperatures of the two sides are both $\gtrsim 3$ keV, in which condition the soft band cooling function is approximately a constant across the shock. Second, the density profile in Eq. 1.4 is based on a spherically symmetric assumption. For real merging shocks, the geometry is more complicated and therefore the density jump could be underestimated especially when the shock plane is not parallel with the LOS. Third, due to the complex geometry, the zero point of r is usually hard to determine in merger systems, and the best-fit result of C is also sensitive to the starting point. Moreover, with only imaging study, a shock front cannot be directly distinguished from a cold front, which also shows a similar surface brightness jump. The observed temperature jumps are less sensitive to the merging geometry and can be used to distinguish shocks from cold fronts. The disadvantage of using temperature jumps for quantifying the shock Mach number is that it requires much more counts to have a robust temperature measurement.

Turbulent velocity dispersion

Quantifying a turbulent Mach number is more difficult than the shock Mach number. The direct way is to measure the turbulent Doppler line broadening. The *Hitomi* telescope first measured the turbulent broadening at the Fe XXV Heα lines in the Perseus Cluster core (Hitomi Collaboration et al. 2016), where the dispersion is < 200 km s^{-1}. Due to the loss of *Hitomi*, currently we do not have instruments for this method. With the performance of the current generation instruments, there are still several indirect ways to quantify the turbulent strength.

For cool core clusters, at the very center of the core region, the density is high enough to have a non-negligible optical depth for a few specific lines with large oscillation strengths, which will lead to resonant scattering of photons emitted from this region, resulting in a suppression of the line strength (Gilfanov et al. 1987). This resonant scattering effect is sensitive to the turbulent velocities, i.e. a higher velocity dispersion results in a lower optical depth. Therefore, the suppression of the line strength is an indicator of the turbulent velocities. Using the RGS grating spectrometer, works by Xu et al. (2002); Werner et al. (2009); de Plaa et al. (2012); Pinto et al. (2016) successfully applied this method on halos from group size to cluster size. See sect. 2 in Gu et al. (2018) for a review on this method.

The method of SB fluctuation power spectrum can also be used for estimating the turbulent velocity dispersions. The theoretical rationale of this

method is that numerical simulations show that for weak turbulence, the turbulent Mach number $\mathcal{M}_{\text{turb}}$ is proportional to the fluctuations of ICM entropy or density (Gaspari & Churazov 2013; Gaspari et al. 2014),

$$\mathcal{M}_{\text{turb,1D}} \propto \frac{\delta\rho}{\rho}. \tag{1.6}$$

Meanwhile, the perturbations of the density field result in SB fluctuations on top of the smoothing varying global cluster emission. Therefore, by computing the power spectrum of the SB fluctuation P_{2D} and inferring the power spectra of the density fluctuation P_{3D} through deprojection, one can estimate the three dimensional density fluctuation (Churazov et al. 2012)

$$A_{\text{3D}} \equiv \frac{\delta\rho}{\rho} = \sqrt{P_{\text{3D}}(k)4\pi k^3}, \tag{1.7}$$

where k is the wavenumber representing a specific scale. Based on the unity slope in Eq. 1.6 (Zhuravleva et al. 2014b), the one dimensional turbulent velocity dispersion is therefore $\sigma_{v,\text{1D}} \equiv \mathcal{M}_{\text{turb,1D}} \times c_{\text{s}} = A_{\text{3D}} \times c_{\text{s}}$.

1.3 Nonthermal views of galaxy clusters

In addition to the stellar component in the cluster galaxies and the thermal emission from the ICM, nonthermal diffuse emission is also detected.

In the γ-ray band, due to the limit of the capabilities of the current γ-ray satellites, the very high energy regime of the cluster field is still little explored. Some detections of excess emission were only reported in the field of the Coma Cluster using *Fermi* data (Ackermann et al. 2016; Xi et al. 2018; Adam et al. 2021; Baghmanyan et al. 2021).

At radio frequencies, the observations of cluster extended radio sources have achieved substantial progress over the past few decades. It turns out that, beside the ubiquitously observed tailed radio galaxies, which have a nature of AGN as the accelerator, other types of extended sources are observed in the fields of galaxy clusters, especially merging clusters. These radio sources have synchrotron nature and steep spectra with spectral index[2] $\alpha < -1$ (e.g. Giovannini et al. 2009; Feretti et al. 2012). Based on the location, morphology, polarization and spectral properties, extended cluster radio sources are classified as radio relics, radio halos and radio

---

[2] $S_\nu \propto \nu^\alpha$

phoenices, where radio relics and radio halos are the two types of most widely observed sources. An example of a galaxy cluster that hosts both radio relics and a radio halo, Abell 2744, is plotted in Fig. 1.5. This example illustrates the differences between radio relics and radio halos in terms of locations, morphologies, spectral properties and polarization properties. A review by van Weeren et al. (2019) presents detailed studies of extended cluster radio sources.

1.3.1 Radio relics

Radio relics, also termed as radio *gischt* (sea spray in German) in early days, are located in the peripheries of clusters. The textbook radio relic in CIZA J2242.8+5301 (the Sausage Cluster) illustrates well the typical properties of radio relics: over one Mpc linear size, spectral flattening at the outer edge, high polarization degree, perpendicularity between polarization electric field vectors and the relic orientation (e.g. van Weeren et al. 2010; Stroe et al. 2013; Hoang et al. 2017; Di Gennaro et al. 2018, 2021). While the Sausage relic is in a perfect arc-like shape, other radio relics show more complex morphology, e.g. the relics in Abell 3667 (Rottgering et al. 1997; de Gasperin et al. 2022), Abell 3376 (Bagchi et al. 2006; Chibueze et al. 2022) and Abell 2256 (Clarke & Ensslin 2006; Kale & Dwarakanath 2010; van Weeren et al. 2012; Rajpurohit et al. 2022). Some galaxy clusters even host a pair of radio relics on the opposite sides of the cluster, e.g. Abell 3667, Abell 3376, Abell 1240 (Bonafede et al. 2009), etc.

1.3.2 Radio halos

Radio halos are located at the center of clusters, overlapping with the ICM emission. Their emissivity is lower than radio relics. Radio halos are unpolarized and have roundish morphologies. The spectral variation across the radio halo is not clear yet. While some sources show uniform spectral indices e.g. the radio halo in the Toothbrush Cluster (van Weeren et al. 2016a; Rajpurohit et al. 2020), other sources show local spectral variation, e.g. the radio halos in Abell 2744 (Rajpurohit et al. 2021) and in the Coma Cluster (Bonafede et al. 2022).

Based on the linear size, there are two subclasses, giant radio halos and mini radio halos. The radii of mini radio halos are usually ~ 100 kpc and up to 300 kpc (e.g. RX J$1347.5 - 1145$, Gitti et al. 2007), while the radii of giant radio halos can be over 1 Mpc. Though they are in distinct sizes, mini

radio halos and giant radio halos have similar orders of magnitude radio power, in which case the two populations are distinguished in the power - radius diagram (Cassano et al. 2008).

1.4   Connecting the nonthermal to the thermal properties

To understand the origins of the cluster extended radio sources, i.e. the cosmic rays (CRs) permeating the ICM, the key is to know the acceleration mechanism and what processes in the structure formation accelerate the CRs. Due to energy losses through synchrotron and inverse Compton emission, the life time of CR is $< 10^8$ yrs, which means that in-situ acceleration mechanisms are required to form the Mpc scale radio sources (Jaffe 1977).

1.4.1   X-ray - radio associations

Radio relics

The idea that extended radio sources in the cluster peripheries are accelerated by shocks is first proposed by Ensslin et al. (1998) and Miniati et al. (2000). The first concrete evidence of a radio relic - X-ray shock association was found in Abell 3667 (Finoguenov et al. 2010). Since then, X-ray shocks at the locations of radio relics have been reported in over ten clusters (e.g. Akamatsu et al. 2015; Eckert et al. 2016; Botteon et al. 2016; Urdampilleta et al. 2018), by which the shock acceleration scenario is therefore confirmed. For many of the radio relics, due to the large projected radii, the ICM density at the relic locations are quite low, which poses difficulty for the detection of the corresponding shock. Moreover, distinguishing a shock front from a cold front requires large number of counts on the low density side for spectral analysis. Shallow X-ray observations could draw a false conclusion, see **Chapter 3** for an example of ZwCl 2341+0000.

The established shock - radio relic connection helps us to better understand the merger configuration, e.g. a double-relic implies a small angle between the merger axis and the sky plane. Meanwhile, numerical simulations of shocks try to explain the observed irregularity of radio relics, e.g. the ring-like relic in Abell 3376 and the filamentary structures in the relic in Abell 2256. The simulation of Skillman et al. (2013) shows the complexity of the shock plane, where the Mach number and magnetic field strength is not uniform. A different viewing angle will result in a different observed
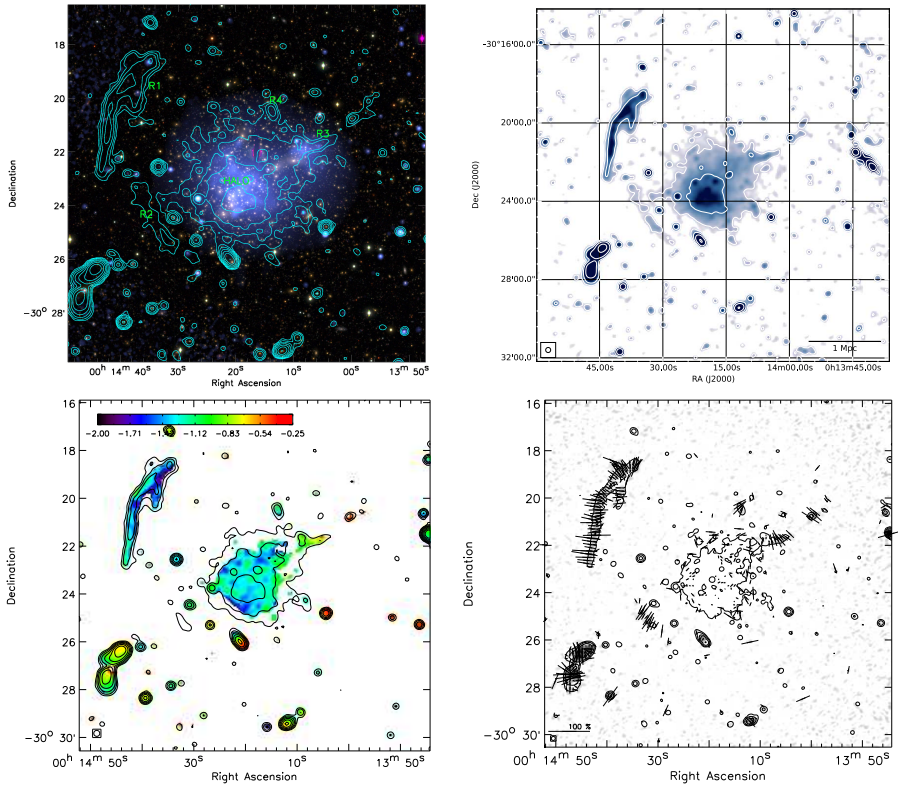
Figure 1.5: Observational properties of radio relics and radio halos, taking Abell 2744 as an example. The figures are adopted from Pearce et al. (2017). *Top left*: The X-ray (blue) and optical composite image overlaid with radio contours. *Top right*: JVLA 1.5 GHz image tapered to $15''$ resolution. *Bottom left:* Spectral map between 1.5 GHz and 3.0 GHz. *Bottom right:* Polarization map of the S band (2 – 4 GHz).

radio morphology. A recent simulation by Dominguez-Fernandez et al. (2021) shows that the shock propagating in a turbulent medium can produce filamentary radio emission.

Radio halos

Radio halos are located at the center of galaxy clusters. The surface intensity of radio halos fades away radially, similar to the SB of the ICM. Analysis of the point-to-point correlation between the radio and the X-ray SB have been performed on many radio halos (e.g. Govoni et al. 2001; Schaal et al. 2016; Rajpurohit et al. 2018; Botteon et al. 2020; Bonafede et al. 2022). These studies find that the SB in the two bands are overall correlated, and the slopes are different between giant radio halos and mini radio halos. In giant radio halos, the slope tends to be sublinear, which means the intensity variation in the radio is shallower than in the X-rays, while mini radio halos show the opposite trend.

Several radio halos have edges associated with X-ray shock or cold fronts. The edge - shock associations are in giant radio halos, e.g. the Coma Cluster (Brown & Rudnick 2011), the Bullet Cluster (Shimwell et al. 2014), Abell 2034 (Shimwell et al. 2016), the Toothbrush Cluster (van Weeren et al. 2016a), as well as a recent new candidate in ClG 0217+70 (see **Chapter 4**). Different from the shock - relic associations, the shocks at the radio halo edges are much closer to the cluster center. It is not yet clear whether the radio edge is formed due to shock acceleration. Associations between cold fronts and radio halo edges have also been reported. They are mainly found in mini halos, where part of the mini radio halo is confined by the sloshing cold fronts, e.g. the Perseus Cluster (Gitti et al. 2002) and Abell 2029 (Govoni et al. 2009). It is also not yet clear whether the subsonic motion of the sloshing cold fronts and the turbulent motions due to the sloshing are responsible for (mildly) accelerating the central CRs.

The occurrence of giant radio halos is also connected to the dynamic status of the cluster. Cassano et al. (2010) studied the relation between X-ray morphology and radio halo occurrence and found that dynamically disturbed clusters are statistically more likely to host a giant radio halo. This bimodality suggests that the turbulence generated by major mergers is the most promising source for accelerating CRs.

1.4.2 Accelerations mechanisms by gas motions

Shock acceleration

CR acceleration in the shock plane is usually described by the diffusive shock acceleration (DSA) theory (Bell 1978a,b; Drury 1983; Blandford & Eichler 1987; Jones & Ellison 1991), where the acceleration process is also known as the first order Fermi process (Fermi 1949). In the DSA theory, when a particle moves from the upstream to the downstream, if the diffusion length is much larger than the thickness of the shock, it will be scattered back and forth across the shock multiple times and will gain energy each time. The accelerated CRs have a power law distribution in the momentum space, $N(p) \propto p^{-\delta}$. Based on the relation between the power law index of CR momentum and the radio spectral index $\alpha = (1 - \delta)/2$, the injected spectral index by the DSA is

$$\alpha_{\mathrm{inj}} = \frac{1}{2} - \frac{\mathcal{M}_{\mathrm{shock}}^2 + 1}{\mathcal{M}_{\mathrm{shock}}^2 - 1}. \tag{1.8}$$

Eq. 1.8 can be applied to spatially resolved radio relics for Mach number estimation. For low resolution radio observations, α_{inj} is usually converted from the integrated spectral index of the entire radio relic, $\alpha_{\mathrm{inj}} = \alpha_{\mathrm{int}} + 0.5$ (Kardashev 1962). However, this injected and integrated spectral index relation is disfavored by recent observations (Stroe et al. 2013; Hoang et al. 2021, also in **Chapter 3**).

One problem of applying DSA to radio relics is that the merging shocks have a low Mach number, $\mathcal{M}_{\mathrm{shock}} \lesssim 3$, where the acceleration efficiency is not sufficient for the observed relic power (Pinzke et al. 2013). The most viable solution is the reacceleration scenario (Markevitch et al. 2005; Kang et al. 2012; Pinzke et al. 2013). In this scenario, due to a preexisting seed population, the weak shock can easily accelerate the aged CR to a Lorentz factor $\gamma \sim 10^4$. The reacceleration scenario can also explain the irregularity of the relic morphology. A recent simulation by ZuHone et al. (2021) shows that the large scale ICM motions can transport aged CRs ejected by AGNs to a large radius. Shocks light these aged CRs up to radio relics and the morphology follows the distribution of the seed population.

Turbulent acceleration

Due to the high β_{pl} of the ICM, the turbulence on large scales is purely hydrodynamic. Once the energy cascade reaches the Alfvén scale l_{A}, the

hydrodynamic turbulence becomes magnetohydrodynamic (MHD) turbulence. MHD turbulence can accelerate CRs through the second order (stochastic) Fermi processes (Fermi 1949), where the momentum change is a second order phenomenon. In these processes, particles can gain or lose energy in each scatter and the probability of gaining energy is higher than losing energy. The second order Fermi processes are milder than the first order Fermi processes. There are several proposed detailed MHD turbulent acceleration mechanisms for the ICM-like plasma, e.g. resonant transit-time damping acceleration and non-resonant acceleration by large scale compressive motions (e.g. Brunetti & Lazarian 2007, 2011).

Due to the mild acceleration efficiency, turbulent acceleration is also unlikely to accelerate CRs from the thermal pool directly. In other words, the MHD turbulence can only reaccelerate the seed CR populations to the energies that produce the observed radio halo emission.

1.5   This thesis

Though we already built up a general picture that radio relics trace cluster merging shocks and radio halos are the results of the subsequent turbulence, there are still many questions unsolved in this field. What is the origin of the discrepancy in shock Mach numbers from X-rays and radio? Is a radio relic always a tracer of merging shocks? Before this thesis work, there was one exception known in the double relic cluster ZwCl 2341+0000, where only 2/3 of the southern relic was associated with an X-ray SB jump (Ogrean et al. 2014). If the edge is a shock and it reaccelerates the CRs for the relic, where does the remaining 1/3 of the relic come from? What parameters in the ICM build up the radio halo power - mass correlation? Is the turbulent Mach number - radio halo power correlation (Eckert et al. 2017) satisfied in samples of different mass ranges and observation frequencies? This thesis aims to better understand these questions starting from X-ray observations. It covers works from case studies to sample study and topics from merging shocks to ICM turbulence. This thesis is structured as follows.

In **Chapter 2**, the detailed analysis of *XMM-Newton* and *Suzaku* observations of Abell 3411 is presented. The cluster Abell 3411 hosts a radio relic that shows a direct evidence of shock reacceleration, where a mild SB jump at the relic location was also detected by *Chandra* (van Weeren et al. 2017). Thanks to the high sensitivity of *XMM-Newton* and the low instru-

mental background of *Suzaku*, we successfully measured the ICM temperature jump across the SB jump and confirmed its shock nature. Meanwhile, a novel method of modeling the soft proton background of the *XMM-Newton* EPIC was presented. This method can successfully reduce the systematics of the soft proton in spectral fitting, especially in the ICM temperature regime of $kT > 4$ keV.

Chapter 3 presents the deep (206 ks) *Chandra* observations of the double radio relic cluster ZwCl 2341+0000 to solve the puzzle of shock - relic connection. The deep observations reveal that the nature of a shock candidate is actually a disrupted cool gas clump. This discovery emphasizes that the shock nature of a SB jump needs to be confirmed with thermodynamic properties of the ICM. The exact location of this shock is suggested by an updated radio spectral index map, where the ICM emission is faint and we can only put a lower limit on the Mach number. In the deep observations, we also discovered a unique cone-like subcluster core remnant. After comparing with numerical simulations, we interpret that this conic structure is in a transition stage between an early blunt-body shape and a late flaring stage, which were previously observed in other systems.

Chapter 4 reports a serendipitous discovery of a galaxy cluster at $z = 0.18$, which is measured using the 6.7 keV Fe XXV Heα lines. The redshift of this cluster was incorrectly estimated as $z = 0.066$ using highly extincted optical data (Brown et al. 2011). With the updated redshift, the radio sources in this cluster show magnificent properties. Among them, one radio relic is located at $r > r_{200}$ and with a linear size > 2 Mpc. The X-ray image also exhibits two SB edges, suggesting a new candidate of radio halo edge - X-ray shock associations. In the subsequent LOFAR radio analysis (Hoang et al. 2021), the two outermost radio relics have a span of 5 Mpc, making this cluster one of the largest separated radio halo - relic system.

Chapter 5 studies the Planck SZ cluster sample in the Low Frequency Array (LOFAR) Two-meter Sky Survey DR2 footprint and focuses on the connections between the ICM properties and the radio halo properties. In this chapter, morphological parameters are calculated as the indicators of cluster dynamic states. Meanwhile, turbulent velocity dispersions are estimated using SB fluctuation power spectra as described in Sect. 1.2.2. Together with the known ICM density profile and temperature, we computed the turbulent dissipation flux in the volumes of the radio halos and find they are correlated with the 150 MHz radio halo power in a unity slope.

This correlation suggests a tight connection between the radio halo power and two ICM properties, i.e. the gas mass in the radio halo volume and the local sound speed determined by the ICM temperature.

1.6 Future prospects

In 2020s, the *XRISM* mission[3] will reopen the window of high resolution imaging X-ray spectroscopy. The imaging spectrometer Resolve will have a < 7 eV spectral resolution to measure the Doppler broadening due to velocity dispersions. Limited by its large point spread function (PSF) size, only nearby high mass clusters are proper candidates for observations. Nevertheless, using a structure function method (e.g. ZuHone et al. 2016), the amplitude and injection scale of the turbulent spectrum can be measured. The high spectral resolution also allow us to better disentangle multitemperature ICM using line diagnostics, by which the post-shock temperature can be better measured.

In one decade, the *Athena* mission will have unprecedented capabilities in both sensitivity and spectral resolution. The high resolution spectrometer X-IFU has a 2.5 eV resolution and will allow us to further explore the velocity structures in the ICM (Roncarelli et al. 2018). Meanwhile, the other instrument WFI has a $40' \times 40'$ field of view. Together with the 10000 cm^2 soft band effective area and the $< 10''$ PSF size, the density fluctuation in the cluster outskirts will be exploited in detail (Bulbul et al. 2019).

---

[3]`https://xrism.isas.jaxa.jp`